Research Article

Wenxiang Ying, Michael A.D. Taylor, and Pengfei Huo*

Resonance Theory of Vibrational Polariton Chemistry at the Normal Incidence

Abstract: We present a theory that explains the resonance effect of the vibrational strong coupling (VSC) modified reaction rate constant at the normal incidence of a Fabry-Pérot (FP) cavity. This analytic theory is based on a mechanistic hypothesis that cavity modes promote the transition from the ground state to the vibrational excited state of the reactant, which is the rate-limiting step of the reaction. This mechanism for a single molecule coupled to a single-mode cavity has been confirmed by numerically exact simulations in our recent work in [J. Chem. Phys. 159, 084104 (2023)]. Using Fermi's golden rule (FGR), we formulate this rate constant for many molecules coupled to many cavity modes inside a FP microcavity. The theory clearly explains the resonance condition for the observed VSC effect and provides a theoretical explanation of why only at the normal incident angle there is the resonance effect, whereas for an oblique incidence, there is no apparent VSC effect for the rate constant even though both cases generate Rabi splitting and forming polariton states.

Keywords: Vibrational Strong Coupling; Polariton Chemistry; Normal Incidence Resonance; Cavity Loss

1 Introduction

Recent experiments [1–6] have demonstrated that chemical reaction rate constants can be suppressed [1–4, 7–9] or enhanced [5, 6, 10] by resonantly coupling molecular vibrations to quantized radiation modes inside a Fabry-Pérot (FP) microcavity [11–13]. This effect has the potential to selectively slow down compet-

ing reactions [3] or speed up a target reaction, thus achieving mode selectivity and offering a paradigm shift in chemistry. Despite extensive theoretical efforts [8, 14–41], the fundamental mechanism and theoretical understanding of the cavity-modified ground-state chemical kinetics remain elusive [14, 42–44]. To the best of our knowledge, there is no unified theory that can explain all of the observed phenomena in the vibrational strong coupling (VSC) experiments [14], including (1) The resonance effect, which happens when the cavity frequency matches the bond vibrational frequency, $\omega_c = \omega_0$, but also only happens when the in-plane photon momentum is $k_\parallel = 0$ (the normal incidence), (2) The collective effect [1, 4, 5] which is the increase in the *magnitude* of VSC modification when increasing the number of molecules N (or concentration $N/\mathcal{V}$), (3) The driving by thermal fluctuations without optical pumping [1, 3]. (4) The isotropic disorder of the dipoles in the cavity, which is assumed in experiments with many molecules [14].

We aim to develop a microscopic theory to explain these observed VSC effects, especially focusing on understanding the resonance effect under normal incidence. Experimentally, only the resonance at normal incidence ($k_\parallel = 0$) gives rise to VSC effects on the rate constant, while a red-detuned cavity that has a light-matter resonance at $k_\parallel > 0$ (oblique incidence) does not give any VSC effect. This observation strongly suggests that forming Rabi splitting is not a *sufficient condition* for achieving the VSC-modified rate effect. Despite recent theoretical progress [18, 45, 46], the resonant condition under normal incidence remains *an unresolved question*.

In this work, we generalized our recently developed analytic Fermi's golden rule (FGR) rate theory of VSC [47] by incorporating many molecules and many cavity modes for both 1D and 2D cases. In particular, we evaluated the photon mode density of states (DOS) inside a 1D FP cavity and found that it gives rise to a van-Hove-type singularity at $k_\parallel = 0$; for a 2D FP cavity, it is found that due to the cavity modes with $k_\parallel > 0$ propagating outside the cavity and caus-

Wenxiang Ying, Department of Chemistry, University of Rochester, 120 Trustee Road, Rochester, New York 14627, USA; wying3@ur.rochester.edu; 0000-0003-3188-020X

Michael A.D. Taylor, The Institute of Optics, Hajim School of Engineering, University of Rochester, Rochester, New York 14627, USA; michael.taylor@rochester.edu; 0000-0002-3300-6834

*Corresponding author: Pengfei Huo, Department of Chemistry, University of Rochester, 120 Trustee Road, Rochester, New York 14627, USA; The Institute of Optics, Hajim School of Engineering, University of Rochester, Rochester, New York 14627, USA; pengfei.huo@rochester.edu; 0000-0002-8639-9299

ing additional cavity loss, the modified photon mode DOS still remains dominant around the bottom of the dispersion band where $k_\parallel = 0$, which are the keys to account for the normal incidence condition of the VSC-modified chemical reaction rate constant. The current theory successfully explains the resonance condition for the observed VSC effect and provides a microscopic understanding of why only at the normal incident angle there is a resonance effect.

2 Model System

Let us consider N identical molecules coupled to many radiation modes inside a FP cavity,

$$
\hat{H} = \sum_{j=1}^{N} \frac{\hat{P}_j^2}{2M} + V(\hat{R}_j) + \hat{H}_\nu + \hat{H}_{\text{loss}}(\hat{q}_{\mathbf{k}}, \hat{x}_{\mathbf{k},\zeta})
$$
$$
+ \sum_{\mathbf{k}} \frac{\hat{p}_{\mathbf{k}}^2}{2} + \frac{\omega_{\mathbf{k}}^2}{2}\Big(\hat{q}_{\mathbf{k}} + \frac{\lambda_c}{\omega_{\mathbf{k}}} \cdot \sum_{j=1}^{N} \mu(\hat{R}_j) \cdot \cos\varphi_j\Big)^2, \quad (1)
$$

where $\hat{R}_j$ is the reaction coordinate for the j_{th} molecule, $V(\hat{R}_j)$ is the ground state potential for each reaction molecule (a double well potential for this paper as is typical for VSC simulations [22, 27, 34, 39]), and $\mu(\hat{R}_j)$ is the dipole associated with the ground electronic state (electronic permanent dipole). In particular, the angle φ_j is the angle between $\hat{\boldsymbol{\mu}}_j$ (the dipole operator of the j_{th} molecule) and the field polarization direction $\hat{\mathbf{e}}$ (we only consider transverse electric (TE) polarization) such that $\hat{\boldsymbol{\mu}}_j \cdot \hat{\mathbf{e}} = \mu(\hat{R}_j)\cos\varphi_j$. A schematic illustration is provided in the top panel of Fig. 1.

The photonic wavevector $\mathbf{k}$ (also referred to as the field propagation direction) has two components, one perpendicular to the cavity mirror $k_\perp$, and the other coplanar with the cavity $k_\parallel$. The FP cavity has the following dispersion relation,

$$
\omega_{\mathbf{k}}(k_\parallel) = \frac{c}{n_c}\sqrt{k_\perp^2 + k_\parallel^2} = \frac{ck_\perp}{n_c}\sqrt{1 + \tan^2\theta}, \quad (2)
$$

where c is the speed of light in vacuum, n_c is the refractive index of the cavity, c/n_c is the speed of the light inside the cavity, and θ is commonly referred to as the incident angle, which is the angle of the photonic mode wavevector $\mathbf{k}$ relative to the norm direction of the mirrors (see the top panel of Fig. 1 for a schematic illustration). In most of the VSC experiments, $n_c \approx 1.5$ for the solution used inside the microcavity. Because $n_c \approx 1$, it will not influence the order of the magnitude
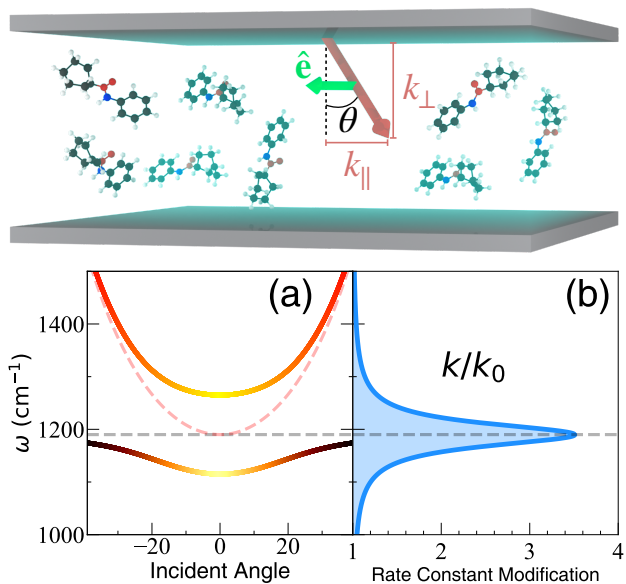

Fig. 1: Top: Schematic illustration of the normal incidence condition for VSC-modified reactions. Bottom: (a) Schematic illustration of the dispersion relations of the cavity (red dashed line), the vibrational energy (gray dashed line), and hybrid polariton states (solid lines). (b) Schematic plot of reaction rate modification as a function of the cavity frequency ω_c.

of our discussion. For simplicity, we explicitly drop n_c throughout this paper. Later, whenever we write c in an expression we should replace it with c/n_c, in principle. When $k_\parallel = 0$ (or $\theta = 0$), the photon frequency is

$$
\omega_c \equiv \omega_{\mathbf{k}}(k_\parallel = 0) = ck_\perp. \quad (3)
$$

The cavity frequency $\omega_{\mathbf{k}}$ in Eq. 1 is associated with the wavevector $\mathbf{k}$, according to Eq. 2. Furthermore, $\hat{q}_{\mathbf{k}} = \sqrt{\hbar/(2\omega_{\mathbf{k}})}(\hat{a}_{\mathbf{k}}^\dagger + \hat{a}_{\mathbf{k}})$ and $\hat{p}_{\mathbf{k}} = i\sqrt{\hbar\omega_{\mathbf{k}}/2}(\hat{a}_{\mathbf{k}}^\dagger - \hat{a}_{\mathbf{k}})$, $\hat{a}_{\mathbf{k}}$ and $\hat{a}_{\mathbf{k}}^\dagger$ are the photonic field annihilation and creation operators for mode $\mathbf{k}$, respectively. The light-matter coupling strength is

$$
\lambda_c = \sqrt{1/(\epsilon_0 \mathcal{V})}, \quad (4)
$$

where ϵ_0 is the effective permittivity inside the cavity and $\mathcal{V}$ is the cavity quantization volume. Each reaction coordinate R_j is coupled to its own local phonon bath described by $\hat{H}_\nu$. Each cavity mode $\hat{q}_{\mathbf{k}}$ couples to its independent bath $\{\hat{x}_{\mathbf{k},\zeta}\}$, accounting for the cavity loss. The cavity modes $\{\hat{q}_{\mathbf{k}}\}$ couple to the dipole of each molecule $\mu(\hat{R}_j)$, where φ_j is the relative angle between the dipole vector and the field polarization direction. Details of the Hamiltonian are provided in the Supplementary Material, Sec. I.

Fig. 1a presents a schematic illustration of the cavity dispersion relation in Eq. 2 (red dashed line). The

molecular excitation dispersion (black dashed line) is insensitive to the incident angle and is a straight line, with energy $\hbar\omega_0$ (see Eq. 7). These two dispersions hybridize due to the light-matter interactions, generating polariton dispersions (the upper and lower branches with solid curves) with the color coding indicating the character of the states, with purely photonic (red), purely vibrational (black), and hybridized (yellow to orange). Fig. 1b presents a schematic illustration of the typical cavity detuning dependence of the rate constant modifications, with the highest intensity of the modification arising at the frequency when $\omega_c = \omega_0$ (resonance condition under normal incidence).

In this paper, we consider a reaction using a thermal barrier crossing model. Fig. 2a presents the first few vibrational states of the double well model, where $|\nu_L\rangle$ denotes the vibrational ground state of the reactant (left well), $|\nu_L'\rangle$ denotes the vibrationally excited state of the reactant, and similar for the product (right well). The red arrow represents the thermal activation process from the vibrational ground state, $|\nu_L\rangle$, to the vibrationally excited state, $|\nu_L'\rangle$ in the reactant well. Then, through the coupling between $|\nu_L'\rangle$ and $|\nu_R'\rangle$, a chemical reaction occurs. Finally, the vibrational excited state $|\nu_R'\rangle$ relaxes to the ground state of the product $|\nu_R\rangle$. The presence of the cavity mode $\hat{q}_{\mathbf{k}}$ explicitly enhances the transition $|\nu_L\rangle \to |\nu_L'\rangle$. The symmetric double-well model [39] is used to model the reaction, with details in Supplementary Material, Sec II. Fig. 2b shows the phonon spectral density $J_\nu(\omega)$ (blue) adapted from Ref. 39 as well as the effective spectral density $J_{\text{eff}}(\omega)$ (red) of the cavity and its associated photon bath environment that accounts for loss. Note that $J_{\text{eff}}(\omega)$ resembles the Brownian oscillator spectral density that centers at a particular frequency. When its peak frequency is in resonance with the quantum vibrational frequency ω_0, $J_{\text{eff}}(\omega)$ could potentially accelerate the state-to-state quantum transitions $|\nu_L\rangle \to |\nu_L'\rangle$ (as indicated by the red arrows in Fig. 2a).

Consider a simplified reaction mechanism outside the cavity as $|\nu_L\rangle \xrightarrow{k_1} |\nu_L'\rangle \xrightarrow{k_2} |\nu_R'\rangle \xrightarrow{k_3} |\nu_R\rangle$. Note that this is the quantum description of the reaction based on quantized states, whereas the classical description is a barrier crossing along the reaction coordinate. These vibrational diabatic states can be directly obtained by computing the eigenspectrum of $V(\hat{R})$ and then diabatizing it. The dominant pathway enhanced by VSC effects is through the first excited states. [47] The simplified mechanism for this reaction is that
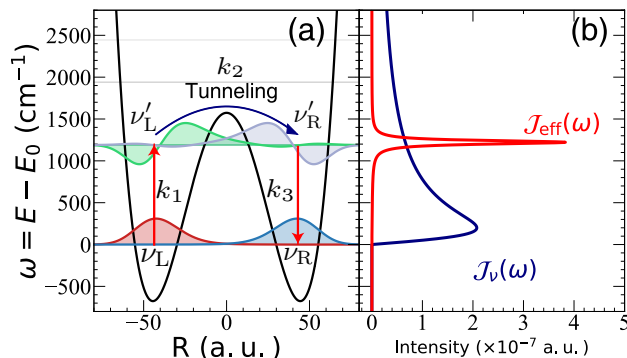

Fig. 2: Potential energy surface for the reaction model. The red arrows represent the thermal activation process from the vibrational ground state, $|\nu_L\rangle$, to the vibrationally excited state, $|\nu_L'\rangle$ in the reactant well (left side of the barrier). Through the coupling between $|\nu_L'\rangle$ and $|\nu_R'\rangle$, a chemical reaction occurs. Finally, the vibrational excited state $|\nu_R'\rangle$ relaxed to the ground state $|\nu_R\rangle$. (b) The effective spectral density $J_{\text{eff}}(\omega)$ (red curve), corresponds to the cavity and its associated loss, compared to the phonon spectral density $J_\nu(\omega)$ (blue).

the thermal activation process causes the transition of $|\nu_L\rangle \to |\nu_L'\rangle$. Then the reaction occurs through the diabatic couplings between $|\nu_L'\rangle$ and $|\nu_R'\rangle$, followed by a vibrational relaxation of the product state, $|\nu_R'\rangle \to |\nu_R\rangle$. The rate-limiting step for the entire process is k_1, where $k_2 \gg k_1$ such that the populations of both $|\nu_L'\rangle$ and $|\nu_R'\rangle$ reach a steady state (plateau in time), and from the steady-state approximation, the overall rate constant for the reaction is $k_0 \approx k_1$. This steady-state behavior of the $|\nu_L'\rangle$ and $|\nu_R'\rangle$ states has recently been verified by numerically exact quantum dynamics simulations [47].

Considering many molecules, we focus on the single excitation subspace. This includes the ground state $|G\rangle$ and N singly excited states $|\nu_j\rangle$ (where $j \in [1, N]$ labels the molecules), defined as

$$|G\rangle \equiv |\nu_L^1\rangle ... \otimes ...|\nu_L^j\rangle \otimes ...|\nu_L^N\rangle, \qquad (5a)$$

$$|\nu_j\rangle \equiv |\nu_L^1\rangle ... \otimes ...|\nu_L'^j\rangle \otimes ...|\nu_L^N\rangle. \qquad (5b)$$

The vibrational transition dipole matrix element is

$$\mu_{LL'} = \langle \nu_L'^j | \mu(\hat{R}_j) | \nu_L^j \rangle, \qquad (6)$$

which is identical for all molecules j. When measuring the absorption spectra of the molecule, the optical response shows a peak at the quantum vibrational frequency

$$\omega_0 = (E_{L'} - E_L)/\hbar. \qquad (7)$$

In the singly excited manifold, the collective "bright state" is expressed as $|B\rangle = \frac{1}{\sqrt{N}} \sum_{k=1}^{N} |\nu_k\rangle$.

The light-matter coupling term, $\propto \sum_{\mathbf{k},j} \hat{q}_{\mathbf{k}} \otimes \mu(\hat{R}_j)$ in Eq. 1, will hybridize the bright state and the photon-dressed ground states, generating the polariton states [48]. When all dipoles are fully aligned, such that $\cos \varphi_j = 1$, and under the resonance condition $\omega_{\mathbf{k}}(k_\parallel) = \omega_0$, the light-matter hybridization generates the upper and lower polariton states (which are light-matter-entangled states) [49] as

$$|\pm_{\mathbf{k}}\rangle = \frac{1}{\sqrt{2}}[|B\rangle \otimes |0_{\mathbf{k}}\rangle \pm |G\rangle \otimes |1_{\mathbf{k}}\rangle], \qquad (8)$$

where $|0_{\mathbf{k}}\rangle$ and $|1_{\mathbf{k}}\rangle$ are photonic Fock states corresponding to the mode with the wavevector, $\mathbf{k}$. The Rabi splitting is the energy difference between the $|+_{\mathbf{k}}\rangle$ and $|-_{\mathbf{k}}\rangle$ states, expressed as

$$\Omega_{\mathrm{R}} = \sqrt{\frac{2\omega_{\mathbf{k}}}{\hbar\epsilon_0}}\sqrt{\frac{N}{\mathcal{V}}}\mu_{\mathrm{LL}'} \equiv 2\sqrt{N}g_{\mathrm{c}} \cdot \sqrt{\omega_{\mathbf{k}}}, \qquad (9)$$

where $g_{\mathrm{c}} = \mu_{\mathrm{LL}'}\sqrt{1/(2\hbar\epsilon_0\mathcal{V})}$ is the Jaynes-Cummings [50] type coupling strength (without the $\sqrt{\omega_{\mathbf{k}}}$-dependence). There are also $N-1$ dark states that do not mix with the photonic degrees of freedom (DOF) under this approximation. Details of this standard analysis are provided in the Supplementary Material, Sec. III.
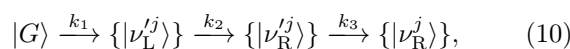
The formation of Rabi splitting/polariton states comes from a collective phenomenon, resulting in the well-known dependence of $\sqrt{N}$ or equivalently $\sqrt{N/\mathcal{V}}$ for Ω_{R}, which has been experimentally confirmed [4]. It has been estimated that there are $N \sim 10^6 - 10^{12}$ molecules effectively coupled to the cavity mode [14, 16, 51] for recent VSC experiments [1, 4], and $\Omega_{\mathrm{R}} \sim 100$ cm^{-1} when $\omega_0 \approx 1000$ cm^{-1} for typical VSC experiments [4, 5]. Despite encouraging progress, what remains largely a mystery is how the collective light-matter coupling can induce the VSC modified rate constant [14]. Another less investigated area [18, 45, 46] is why forming polaritons at a finite incident angle does not necessarily lead to the change of the VSC kinetics, and the only observed VSC effects occur at $k_\parallel = 0$ (or $\theta = 0$).

3 Theoretical Results

3.1 Analytic Rate Constant Expression

To provide a microscopic mechanism of VSC-modified reactions, we *hypothesize* that the cavity modes enhance the transition from ground states to a vibrationally excited state manifold of the reactant, leading to an enhancement of the *steady-state population* of both the delocalized states on the reactant side and the excited states manifold on the product side (right well) $\{|\nu_{\mathrm{R}}'^j\rangle\}$, which then relax to the vibrational ground state manifold on the product side (right well), $\{|\nu_{\mathrm{R}}^j\rangle\}$. For a single molecule strongly coupled to a single cavity mode, our numerical simulations [47] have confirmed the validity of this hypothesis. The proposed reaction mechanism is represented below

$$|G\rangle \xrightarrow{k_1} \{|\nu_{\mathrm{L}}'^j\rangle\} \xrightarrow{k_2} \{|\nu_{\mathrm{R}}'^j\rangle\} \xrightarrow{k_3} \{|\nu_{\mathrm{R}}^j\rangle\}, \qquad (10)$$

among which $k_1 \ll k_2, k_3$.

When the molecular system is originally in the Kramers low friction regime (before the Kramers turnover [52, 53], or the so-called energy diffusion-limited regime), the cavity enhancement of the rate constant k_1 will occur [30–32, 34, 35, 39]. This has been extensively discussed in recent theoretical work [39, 47]. When explicitly assuming that $k_1 \ll k_2, k_3$, then $|G\rangle \xrightarrow{k_1} \{|\nu_{\mathrm{L}}'^j\rangle\}$ is the *rate limiting step*, and the population of intermediate states will reach a steady-state behavior. As such, due to the steady-state approximation, the overall rate constant is [47]

$$k \approx k_1 = k_0 + k_{\mathrm{VSC}} \ll k_2, k_3, \qquad (11)$$

where k_0 is the chemical reaction rate constant outside the cavity, and k_{VSC} accounts for the pure cavity-induced effect. As this is a thermally activated reaction, there already exist some excited-state populations and transitions outside the cavity, which k_0 accounts for. Note that Eq. 11 assumes that the pure cavity effect k_{VSC} can be added with k_0, which is a *fundamental assumption* in the current theory.

To quantitatively express k_{VSC}, we analyze the overall effect of the cavity and the photon loss environment on molecular systems by performing a normal mode transformation [54–56] to the Hamiltonian in Eq. 1 and obtaining an effective Hamiltonian, where now the cavity modes $\{\hat{q}_{\mathbf{k}}\}$ and the photon loss bath modes $\{\hat{x}_{\mathbf{k},\zeta}\}$ (described by $\hat{H}_{\mathrm{loss}}$) are transformed into effective photonic normal mode coordinates $\{\hat{\tilde{x}}_{\mathbf{k},\zeta}\}$, which are collectively coupled to the system DOF through the following term,

$$\hat{H}_{\mathrm{LM}} = \hat{S} \otimes \sum_{\mathbf{k}} \hat{\mathcal{F}}_{\mathbf{k}}, \qquad (12)$$

where $\hat{S} \equiv \sum_{j=1}^N \mu(\hat{R}_j) \cdot \cos \varphi_j$ is the collective system operator, $\hat{\mathcal{F}}_{\mathbf{k}} = \sum_\zeta \tilde{c}_{\mathbf{k},\zeta}\hat{\tilde{x}}_{\mathbf{k},\zeta}$ is the stochastic force exerted by the $\mathbf{k}$-th effective bath, $\{\hat{\tilde{x}}_{\mathbf{k},\zeta}\}$ are the normal modes of $\{\hat{q}_{\mathbf{k}}, \hat{x}_{\mathbf{k},\zeta}\}$, and the coupling constants $\tilde{c}_{\mathbf{k},\zeta}$ as

well as bath frequencies $\tilde{\omega}_{\mathbf{k},\zeta}$ are characterized by an effective spectral density,

$$J_{\text{eff}}(\omega_{\mathbf{k}}, \omega) = \frac{\lambda_{\text{c}}^2 \omega_{\mathbf{k}}^2 \tau_{\text{c}}^{-1} \omega}{\left(\omega_{\mathbf{k}}^2 - \omega^2\right)^2 + \tau_{\text{c}}^{-2} \omega^2}, \qquad (13)$$

where τ_{c} is the cavity lifetime. Detailed derivation is provided in Supplementary Material, Sec. IV.

The rate constant change k_{VSC} in Eq. 11 originates from a purely cavity-induced effect, which promotes the transition from $|G\rangle$ to the singly excited states manifold $\{|\nu_j\rangle\}$. Note that the light-matter coupling term in Eq. 12 suggests that through the collective coupling between all molecules and the cavity modes, the cavity operators $\hat{\mathcal{F}}_{\mathbf{k}}$ will mediate the transition. We use FGR to estimate this transition rate constant. The coupling for this quantum transition is provided by $\hat{\mathcal{S}}$, and the transition is mediated by the effective photon bath operators $\hat{\mathcal{F}}_{\mathbf{k}}$ with their spectral densities $J_{\text{eff}}(\omega_{\mathbf{k}}, \omega)$ in Eq. 13. Using FGR to estimate the transition with the frequency $\omega = \omega_0$ (the $|G\rangle \xrightarrow{k_1} \{|\nu_{\text{L}}^{\prime j}\rangle\}$ transition), and assumed that the pathways are completely independent (*i.e.*, no interference between pathways), we have the following expression for the overall reaction rate constant,

$$\begin{aligned} k_{\text{VSC}} &= \frac{1}{N} \frac{2}{\hbar} \sum_{j=1}^{N} \left|\langle \nu_j | \hat{\mathcal{S}} | G \rangle\right|^2 \cdot \sum_{\mathbf{k}} \mathcal{P}_{\mathbf{k}} \cdot J_{\text{eff}}(\omega_{\mathbf{k}}, \omega_0) \cdot n(\omega_0) \\ &= \frac{4}{N} g_N^2 \cdot \sum_{\mathbf{k}} \mathcal{P}_{\mathbf{k}} \cdot \frac{\omega_{\mathbf{k}}^2 \tau_{\text{c}}^{-1} \omega_0}{\left(\omega_{\mathbf{k}}^2 - \omega_0^2\right)^2 + \tau_{\text{c}}^{-2} \omega_0^2} \cdot n(\omega_0), \end{aligned} \tag{14}$$

with detailed derivation provided in Sec. V of the Supplementary Material. In Eq. 14, the $1/N$ factor accounts for the normalized rate constant per molecule, and the collective Jaynes-Cummings-type coupling strength g_N^2 (without cavity frequency dependence) is defined as

$$g_N^2 \equiv \frac{1}{2\hbar\epsilon_0 \mathcal{V}} \sum_{k=1}^{N} \left|\langle \nu_k | \hat{\mathcal{S}} | G \rangle\right|^2. \tag{15}$$

When all molecules are aligned with the cavity polarization direction, $g_N^2 = N g_{\text{c}}^2$ (cf. Eq. 9). Furthermore,

$$n(\omega_0) = 1/(e^{\beta\hbar\omega_0} - 1) \approx e^{-\beta\hbar\omega_0} \tag{16}$$

is the Bose-Einstein distribution function, where $\beta = 1/k_{\text{B}}T$ with k_{B} as the Boltzmann constant and T as the temperature. For the typical parameters in VSC experiments, $\omega_0 \approx 1200 \text{ cm}^{-1}$ and room temperature $1/\beta = k_{\text{B}}T \approx 200 \text{ cm}^{-1}$, such that $\beta\hbar\omega_0 \gg 1$. Finally,

$\mathcal{P}_{\mathbf{k}}$ represents the thermal weighting factor for accessing the cavity mode $\omega_{\mathbf{k}}$, with

$$\mathcal{P}_{\mathbf{k}} = \frac{e^{-\beta\hbar\omega_{\mathbf{k}}}}{\mathcal{Z}}, \tag{17}$$

and $\mathcal{Z}$ is the normalization factor such that $\sum_{\mathbf{k}} \mathcal{P}_{\mathbf{k}} = 1$.

We further define the accumulated spectral function as follows (cf. Eq. 14)

$$\mathcal{A}(\omega) \equiv \frac{1}{\mathcal{Z}} \sum_{\mathbf{k}} \frac{\omega_{\mathbf{k}}^2 \tau_{\text{c}}^{-1} \omega}{\left(\omega_{\mathbf{k}}^2 - \omega^2\right)^2 + \tau_{\text{c}}^{-2} \omega^2} \cdot e^{-\beta\hbar\omega_{\mathbf{k}}}, \tag{18}$$

and k_{VSC} in Eq. 14 can then be written as

$$k_{\text{VSC}} = \frac{4}{N} g_N^2 \cdot \mathcal{A}(\omega_0) \cdot n(\omega_0). \tag{19}$$

3.2 The Resonance Effect at the Normal Incidence

Next, we work to provide an analytic expression of $\mathcal{A}(\omega)$ for the 1D and 2D FP cavities, which is one of the *main theoretical results* of this work. Under the continuous $k_\parallel$ limit, one can replace the sum in Eq. 18 with an integral as follows

$$\sum_{\mathbf{k}} f(\omega_{\mathbf{k}}) \to \int d\omega_{\mathbf{k}} \; g_{\text{D}}(\omega_{\mathbf{k}}) f(\omega_{\mathbf{k}}), \tag{20}$$

where $g_{\text{D}}(\omega_{\mathbf{k}})$ is the DOS of the modes inside a D-dimensional FP cavity, defined as

$$g_{\text{D}}(\omega_{\mathbf{k}}) = \frac{1}{N_{\text{D}}} \int dk^{\text{D}} \; \delta(\omega - \omega_{\mathbf{k}}), \tag{21}$$

where N_{D} is the normalizing constant. Eq. 21 can be evaluated by using the dispersion relation in Eq. 2.

For the one-dimensional FP cavity [46], if we ignore the influence of cavity loss ($\hat{H}_{\text{loss}}$ in Eq. 1), one can show that the DOS for the photonic modes (D = 1) is expressed as

$$g_{\text{1D}}(\omega_{\mathbf{k}}) = \frac{\omega_{\mathbf{k}}}{k_\parallel^{\text{m}} \sqrt{\omega_{\mathbf{k}}^2 - \omega_{\text{c}}^2}} \cdot \Theta(\omega_{\mathbf{k}} - \omega_{\text{c}}), \tag{22}$$

where $k_\parallel^{\text{m}}$ is the cutoff value of the in-plane wavevector, and $\Theta(\omega_{\mathbf{k}} - \omega_{\text{c}})$ is the Heaviside step function. The details of the derivations are provided in the Supplementary Material, Sec. VI. The DOS, $g_{\text{1D}}(\omega_{\mathbf{k}})$, in Eq. 22 has a singularity at $\omega_{\mathbf{k}} = \omega_{\text{c}}$, which is known as (the first type of) the van-Hove-type singularity [57]. Such a concentrated peak in the $g_{\text{1D}}(\omega)$ at $\omega = \omega_{\text{c}}$ has been numerically observed in Fig. 1 of Ref. 46. We will turn to the case of including the effects of cavity loss in the in-plane direction at the end of this section.
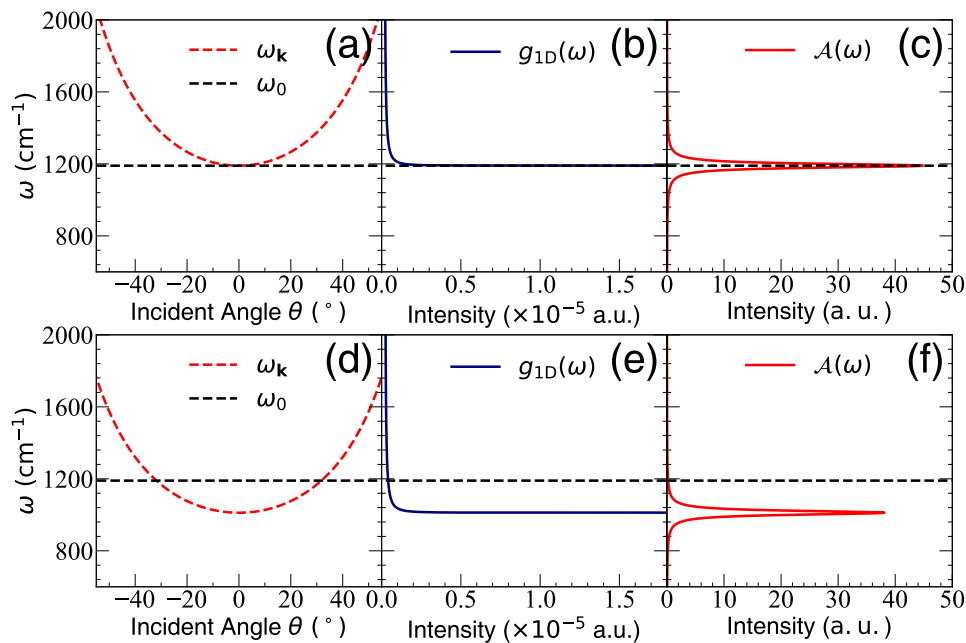
Fig. 3: (a) The cavity dispersion relation (Eq. 2), (b) the schematic 1D DOS $g_{1D}(\omega)$ (Eq. 22) and (c) the accumulated spectral function $\mathcal{A}(\omega)$ (Eq. 18, evaluated using Eq. 23) for the normal incidence case $\omega_c = \omega_0$, where the resonance condition is reached at $\theta = 0$. (d)-(f) corresponds to the red-detuned case (oblique incidence), with $\omega_c = 0.85\,\omega_0$, whose resonance condition is reached at $\theta \approx 32°$. The cavity lifetime is taken as $\tau_c = 200$ fs.

Using Eq. 22 and replacing the sum in Eq. 18 as an integral, we have

$$\mathcal{A}(\omega_0) = \frac{1}{\mathcal{Z}} \sum_{\mathbf{k}} \frac{\omega_{\mathbf{k}}^2 \tau_c^{-1} \omega_0}{\left(\omega_{\mathbf{k}}^2 - \omega_0^2\right)^2 + \tau_c^{-2}\omega_0^2} \cdot e^{-\beta\hbar\omega_{\mathbf{k}}} \quad (23)$$

$$= \frac{1}{\mathcal{Z}} \int d\omega_{\mathbf{k}}\, g_{1D}(\omega_{\mathbf{k}}) \frac{\omega_{\mathbf{k}}^2 \tau_c^{-1} \omega_0}{\left(\omega_{\mathbf{k}}^2 - \omega_0^2\right)^2 + \tau_c^{-2}\omega_0^2} \cdot e^{-\beta\hbar\omega_{\mathbf{k}}}$$

$$= \frac{1}{\mathcal{Z}} \int_{\omega_c}^{\omega_m} d\omega_{\mathbf{k}}\, \frac{\omega_{\mathbf{k}}}{k_{\parallel}^m \sqrt{\omega_{\mathbf{k}}^2 - \omega_c^2}} \frac{\omega_{\mathbf{k}}^2 \tau_c^{-1} \omega_0}{\left(\omega_{\mathbf{k}}^2 - \omega_0^2\right)^2 + \tau_c^{-2}\omega_0^2} \cdot e^{-\beta\hbar\omega_{\mathbf{k}}}$$

$$\approx \frac{\omega_c^2 \tau_c^{-1} \omega_0}{\left(\omega_c^2 - \omega_0^2\right)^2 + \tau_c^{-2}\omega_0^2},$$

where $\omega_m = c\sqrt{k_{\perp}^2 + (k_{\parallel}^m)^2}$ is the cutoff frequency. In the last line of Eq. 23, we take the limit of $k_{\parallel}^m \to \infty$ when evaluating the integral, which gives a finite value despite the singularity in $g_{1D}(\omega_{\mathbf{k}})$ because only the contribution from $\omega_{\mathbf{k}} = \omega_c$ survives. At the same time, $\mathcal{Z} = \sum_{\mathbf{k}} \mathcal{P}_{\mathbf{k}} = \int d\omega_{\mathbf{k}}\, g_{1D}(\omega_{\mathbf{k}}) e^{-\beta\hbar\omega_{\mathbf{k}}} \approx e^{-\beta\hbar\omega_c}$, so $1/\mathcal{Z}$ cancels the $e^{-\beta\hbar\omega_c}$ factor that arises from the integral. The above theoretical results also justify the commonly used single mode approximation in investigating VSC reactivities [22, 27, 39] because only the mode with frequency ω_c survives. Using the expression of $\mathcal{A}(\omega_0)$ (Eq. 23) in the rate constant expression of Eq. 19 and taking the limit of $N = 1$, one obtains the previous re-

sult of k_{VSC} (see Eq. 32) for a single molecule coupled to a single mode in Ref. 47.

Fig. 3 presents the cavity dispersion relation of $\omega_{\mathbf{k}}(\theta)$ (see Eq. 2) in panels (a) and (d), the 1D DOS $g_{1D}(\omega)$ (see Eq. 22) in panels (b) and (e), and the accumulated spectral function $\mathcal{A}(\omega)$ (see Eq. 18) which is directly proportional to k_{VSC} in panels (c) and (f). In panels (a)-(c), one can clearly see that under the normal incident condition $\omega_{\mathbf{k}} = \omega_0$ at $\theta = 0$, $\mathcal{A}(\omega)$ is maximized at $\omega_c = \omega_0$ and accordingly, the rate constant will also maximize based on the FGR expression (Eq. 14). In the detuned case ($\omega_c \neq \omega_0$ or $|\theta| > 0$) in panels (d)-(f), the intensity of $\mathcal{A}(\omega)$ still peaks at $\theta = 0$, but the value of $\mathcal{A}(\omega_0)$ diminishes at the "resonance condition" $\omega_{\mathbf{k}} = \omega_0$ (for generating Rabi splitting).

This analysis also provides a possible explanation for the resonance effect at normal incidence ($k_{\parallel} = 0$) for a 1D FP cavity. In Eq. 23, it is clear that the peak of this function is located at $\omega_c = \omega_0$ for $k_{\parallel} = 0$. Thus, the VSC-modified rate constant occurs only when $\omega_c = \omega_0$. This is because there is a van-Hove-type singularity [57] in the 1D DOS, $g_{1D}(\omega_{\mathbf{k}})$, which manifests itself as the $1/\sqrt{\omega_{\mathbf{k}}^2 - \omega_c^2}$ term in Eq. 23, such that the integral only survives and gives a finite value at $\omega_{\mathbf{k}} = \omega_c$, and at $\omega_{\mathbf{k}} > \omega_c$, the integral becomes vanishingly small.

However, directly extending this simple consideration for the DOS cannot explain the normal incidence condition for a 2D FP cavity (when only considering the TE polarization direction). This is because the 2D DOS $g_{2D}(\omega_\mathbf{k})$ does not have any singularity. Specifically, the DOS for the photonic modes inside a 2D FP cavity is expressed as

$$g_{2D}(\omega_\mathbf{k}) = \frac{1}{2\pi\xi}\omega_\mathbf{k} \cdot \Theta(\omega_\mathbf{k} - \omega_c), \quad (24)$$

where the normalization factor ξ is

$$\xi(k_\parallel^m) = \frac{1}{3}\{[k_\perp^2 + (k_\parallel^m)^2]^{3/2} - k_\perp^3\}, \quad (25)$$

which explicitly depends on $k_\parallel^m$ the in-plane cutoff. See Sec. VI of the Supplementary Material for more details.

For the 2D cavity case, one needs to consider beyond the simple density of state argument. Note that the loss associated with the lifetime τ_c only considers the loss in the $k_\perp$ direction. What we have not explicitly considered before was the cavity loss along the $k_\parallel$ direction due to the photon propagating outside the cavity. When $k_\parallel \neq 0$, the photon propagation along the in-plane direction will cause additional loss, due to the photon propagating outside the effective coupling area. Let $\mathcal{D}$ be the diameter of the quantization area (along the $k_\parallel$ direction in Fig. 1) and $\mathcal{L}$ be the mirror distance (along the $k_\perp$ direction in Fig. 1), so the effective cavity quantization volume $\mathcal{V} = \mathcal{L} \cdot \mathcal{D}^2$. The mode lifetime can be estimated as

$$\tau_\parallel(k_\parallel) = \frac{\mathcal{D}}{c \cdot \sin\theta} = \frac{\mathcal{D}\sqrt{k_\perp^2 + k_\parallel^2}}{c \cdot k_\parallel} = \frac{\mathcal{D}}{c^2} \cdot \frac{\omega_\mathbf{k}}{k_\parallel}, \quad (26)$$

which is propotional to $k_\parallel^{-1}$ when $k_\parallel \ll k_\perp$, and the associated loss rate is $\Gamma_{10}' = 1/\tau_\parallel$ (which corresponding to the photon decay of $|1_\mathbf{k}\rangle \to |0_\mathbf{k}\rangle$). Note that $\tau_\parallel$ differs from the cavity lifetime τ_c introduced previously. Specifically, $\tau_\parallel$ accounts for loss in the in-plane direction, τ_c describes the loss channel *only* due to the escaping of the photon with a direction that is perpendicular to the mirror surface $k_\perp$, and was introduced through the $\hat{H}_{loss}$ term and was assumed to be identical for all cavity modes $\omega_\mathbf{k}$ (independent of $k_\parallel$). A reasonable estimation for $\mathcal{D}$ is provided as follows. As mentioned before, the typical values for the VSC experiments are $N \approx 10^6 \sim 10^{12}$ [14, 16, 51], and the effective density is $N/\mathcal{V} \approx 10^{20}$ cm^{-3} [58]. Using $\mathcal{V} = \mathcal{L} \cdot \mathcal{D}^2$, and the typical value for the mirror distance $\mathcal{L} = 1$ μm, we have $\mathcal{D} \approx 10^{-1} \sim 10$ μm (or $10^2 \sim 10^5$ nm), and the range of $\mathcal{D}/c \approx 1 \sim 100$ fs. For example, when $\mathcal{D} \sim 300$ nm,

$\mathcal{D}/c \sim 10^{-15}$ s$^{-1} = 1$ fs. On the other hand, τ_c usually varies from 100 fs [3] to 5 ps [59] in typical VSC experiments.

Note that the term $e^{-\beta\hbar\omega_\mathbf{k}}$ in Eq. 18 originates from the photon field thermal distribution, which can also be interpreted as the ratio between two photonic transitions rate constants

$$e^{-\beta\hbar\omega_\mathbf{k}} = \Gamma_{01}/\Gamma_{10}, \quad (27)$$

where Γ_{01} is the rate for the $|0_\mathbf{k}\rangle \to |1_\mathbf{k}\rangle$ photonic Fock states transition due to thermal excitation, and $\Gamma_{10} = 1/\tau_c$ is the cavity loss rate along the $k_\perp$ direction (associated with $|1_\mathbf{k}\rangle \to |0_\mathbf{k}\rangle$), which was assumed to be identical for all $\mathbf{k}$ modes. To effectively account for the additional photon loss associated with the $k_\parallel$ direction, we modify the detailed balance relation by replacing the original $e^{-\beta\hbar\omega_\mathbf{k}}$ with $\mathcal{P}_{eff}(\omega_\mathbf{k})$, defined as follows.

$$\mathcal{P}_{eff}(\omega_\mathbf{k}) = \frac{\Gamma_{01}}{\Gamma_{10} + \Gamma_{10}'} = \frac{\tau_c^{-1}e^{-\beta\hbar\omega_\mathbf{k}}}{\tau_c^{-1} + \tau_\parallel^{-1}}, \quad (28)$$

where $\tau_\parallel$ (defined in Eq. 26) is $k_\parallel$-dependent. This can also be seen as putting a $\tau_c^{-1}/(\tau_c^{-1} + \tau_\parallel^{-1})$ correction factor, where $\tau_\parallel$ explicitly depends on $k_\parallel$ (Eq. 26). As expected, when $k_\parallel = 0$, $\tau_\parallel^{-1} = 0$, one should have $\mathcal{P}_{eff}(\omega_\mathbf{k}) \to e^{-\beta\hbar\omega_\mathbf{k}}$. Further, the normalization factor is also modified as $\mathcal{Z} \to \mathcal{Z}_{eff} = \sum_\mathbf{k} \mathcal{P}_{eff}(\omega_\mathbf{k})$.

Using $\mathcal{P}_{eff}(\omega_\mathbf{k})$ in Eq. 28, the accumulated spectral function $\mathcal{A}(\omega_0)$ is modified as

$$\mathcal{A}(\omega_0) = \frac{1}{\mathcal{Z}_{eff}} \sum_\mathbf{k} \frac{\omega_\mathbf{k}^2 \tau_c^{-1}\omega_0}{(\omega_\mathbf{k}^2 - \omega_0^2)^2 + \tau_c^{-2}\omega_0^2} \cdot \mathcal{P}_{eff}(\omega_\mathbf{k}) \quad (29)$$

$$= \frac{1}{\mathcal{Z}_{eff}} \int d\omega_\mathbf{k} \, g_{2D}(\omega_\mathbf{k}) \frac{\omega_\mathbf{k}^2 \tau_c^{-1}\omega_0}{(\omega_\mathbf{k}^2 - \omega_0^2)^2 + \tau_c^{-2}\omega_0^2} \cdot \mathcal{P}_{eff}(\omega_\mathbf{k})$$

$$= \frac{1}{\mathcal{Z}_{eff}} \frac{1}{2\pi\xi} \int_{\omega_c}^{\omega_m} d\omega_\mathbf{k} \, \frac{\omega_\mathbf{k} \cdot \Gamma_{01}}{\Gamma_{10} + \Gamma_{10}'} \cdot \frac{\omega_\mathbf{k}^2 \tau_c^{-1}\omega_0}{(\omega_\mathbf{k}^2 - \omega_0^2)^2 + \tau_c^{-2}\omega_0^2},$$

where the weighting factor $\omega_\mathbf{k}\Gamma_{01}/(\Gamma_{10} + \Gamma_{10}')$ in the above expression takes a sharp maximum at $k_\parallel = 0$ and decays quickly when $k_\parallel$ increases, because Γ_{10}' increases quickly as $k_\parallel$ increases. This means that for a 2D cavity, as used in all existing VSC experiments, the VSC-modified rate constant is still maximized around $\omega_\mathbf{k}(k_\parallel = 0) = \omega_c = \omega_0$, fulfilling the normal incidence condition. Note that the above correction factor $\Gamma_{01}/(\Gamma_{10} + \Gamma_{10}')$ can also be applied to the 1D FP cavity but does not introduce any difference in Fig. 3, due to the van-Hove singularity in the DOS (see Eq. 22) which dominates the entire integral, forcing $\mathcal{P}_{eff}(\omega_\mathbf{k}) \to e^{-\beta\hbar\omega_\mathbf{k}}$ (as $\tau_\parallel \to \infty$ when $k_\parallel = 0$).
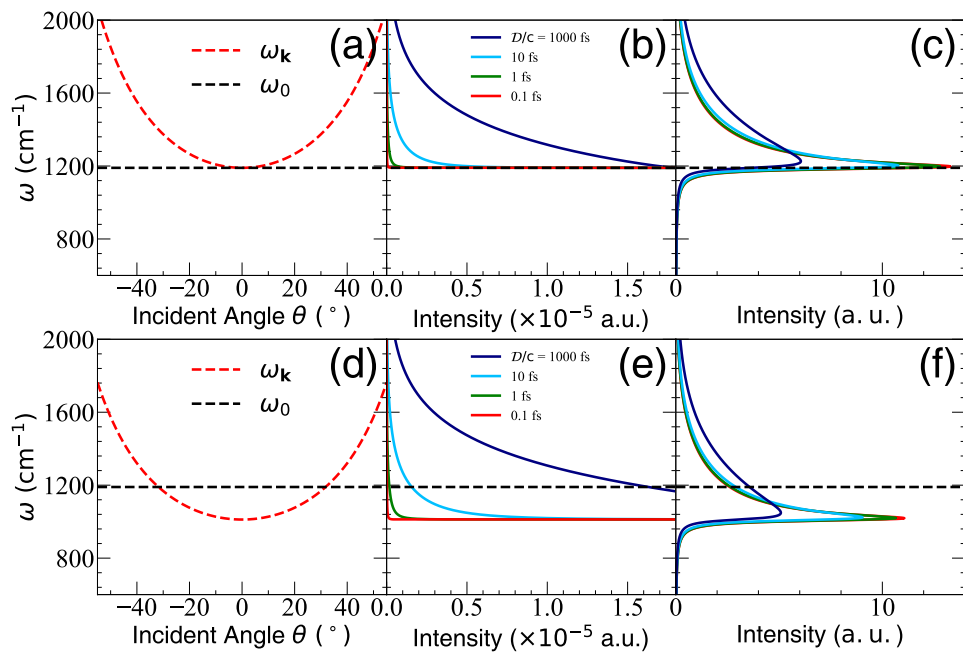
Fig. 4: Same as Fig. 3, but with a 2D FP cavity. (a) Same as Fig. 3a. (b) The weighting factor $\omega_{\mathbf{k}}\Gamma_{01}/(\Gamma_{10} + \Gamma'_{10})$ under different $\mathcal{D}/c$ values, where $\mathcal{D}/c = 0.1$ fs corresponds to $\mathcal{D} \approx 0.03\mu$m, $\mathcal{D}/c = 1000$ fs corresponds to $\mathcal{D} \approx 300 \ \mu$m. (c) The accumulated spectral function $\mathcal{A}(\omega)$ (see Eq. 18) for the normal incidence case $\omega_{\mathrm{c}} = \omega_0$, where the resonance condition is reached at $\theta = 0$. (d)-(f) corresponds to the red-detuned case (oblique incidence), with $\omega_{\mathrm{c}} = 0.85 \ \omega_0$, whose resonance condition is reached at $\theta \approx 32°$. The cavity lifetime is taken as $\tau_{\mathrm{c}} = 200$ fs.

Fig. 4 presents the cavity dispersion relation of $\omega_{\mathbf{k}}(\theta)$ (see Eq. 2) in panels (a) and (d), the weighting factor $\omega_{\mathbf{k}}\Gamma_{01}/(\Gamma_{10} + \Gamma'_{10})$ in panels (b) and (e), and the accumulated spectral function $\mathcal{A}(\omega)$ (see Eq. 29) for the 2D cavity case in panels (c) and (f). Fig. 4b shows the numerical behavior of the weighting factor $\omega_{\mathbf{k}}\Gamma_{01}/(\Gamma_{10} + \Gamma'_{10})$ under different $\mathcal{D}/c$ values (see Eq. 26), among which $\mathcal{D}/c = 1000$ fs, 10 fs, 1 fs, and 0.1 fs, corresponding to $\mathcal{D} = 3 \times 10^5$ nm, 3×10^3 nm, 300 nm, and 30 nm, respectively. All are within the reasonable range of $\mathcal{D}$ values discussed previously. One can see that the maximal contribution still comes from $k_{\parallel} = 0$, although no singularity is present. Moreover, the width becomes narrower as $\mathcal{D}/c$ decreases. Note that $c/\mathcal{D}$ is usually a very large quantity, so that when the incident angle θ is slightly larger, $\Gamma'_{10} \gg \Gamma_{10}$ becomes dominant in cavity loss.

Fig. 4c presents the behavior of the accumulated spectral function $\mathcal{A}(\omega)$, which is calculated by evaluating Eq. 29 numerically using trapezoidal integration within the region of $\omega_{\mathrm{c}} \leq \omega_{\mathbf{k}} \leq 5\omega_{\mathrm{c}}$ using 4×10^6 grid points, where numerical convergence is carefully checked. One can see that $\mathcal{A}(\omega)$ peaks at $\omega > \omega_{\mathrm{c}}$ when $\mathcal{D}/c$ is large, and gradually moves to $\omega = \omega_{\mathrm{c}}$ when $\mathcal{D}/c$ decreases and Γ'_{10} dominates the cavity loss for $k_{\parallel} > 0$.

Additionally, compared to Fig. 3c, here $\mathcal{A}(\omega)$ tails toward the higher energy. This is because the weighting factor $\omega_{\mathbf{k}}\Gamma_{01}/(\Gamma_{10} + \Gamma'_{10})$ is not truly singular at ω_{c}. The smaller the $\mathcal{D}/c$ value, the sharper $\mathcal{A}(\omega)$ will be. When taking the limit of $\mathcal{D}/c \to 0$, Fig. 4c reduces back to Fig. 3c. On the other hand, when $\mathcal{D}/c \to \infty$, there will be no loss in the in-plane direction, corresponding to a much wider $\mathcal{A}(\omega)$ (see the dark blue curve in Figs. 4c and f), which is only bounded by $e^{-\beta\hbar\omega_{\mathbf{k}}}$. Under this condition, $\mathcal{A}(\omega)$ still peaks at a particular frequency, but with $\omega_{\mathrm{c}} > \omega_0$. Fig. 4d-f corresponds to the red-detuned case under oblique incidence, where $\omega_{\mathrm{c}} = 0.85\omega_0$.

With the above analysis, we have theoretically justified why the VSC-modified chemical kinetics only occurs at the normal incidence when $\omega_{\mathrm{c}} = \omega_0$ for a 2D FP cavity, which agrees with experimental observations [1, 11–13]. This is because even though there is no singularity in $g_{2\mathrm{D}}(\omega)$, the cavity loss along the $k_{\parallel}$ direction forces the cavity spectra function $\mathcal{A}(\omega)$ to peak up at $\omega = \omega_{\mathrm{c}}$, which forces the normal incidence condition. The condition for observing Rabi splitting (see Eq. 9), on the other hand, is $\omega_{\mathbf{k}} = \omega_{\mathrm{c}}\sqrt{1 + \tan^2\theta} = \omega_0$ for any $\theta \geq 0$. Although the modes with $\theta > 0$ barely contribute to k_{VSC}, the mode density is *finite* (see Fig. 3e)

and for $\omega_0 > \omega_c$ there will *always* be a mode available that satisfies $\omega_{\mathbf{k}} = \omega_0$, generating Rabi splitting at $\theta > 0$. As such, the theory provides a clear understanding of the fundamental difference between the condition for forming the Rabi splitting and that of the VSC resonance modification of the rate constant. This explains the experimentally observed resonance phenomena [11, 14] that occur only at $\omega_c = \omega_0$ at the normal incident angle when $k_{\parallel} = 0$ (or $\theta = 0$), but not at a finite angle of θ even though the resonance condition for generating Rabi splitting is fulfilled.

3.3 No Apparent Collective Effect.

For our discussion on collectivity, we begin by considering the FGR expression in Eq. 14. If all the molecules' dipoles are perfectly aligned with the cavity polarization, then $\cos\varphi_j = 1$ for all molecules, j, and $\hat{\mathcal{S}} = \sum_j \mu(\hat{R}_j)$. For simplicity, we just focus on the 1D cavity case, since for 2D cavity there is no apparent collective effect either. Evaluating Eq. 19 using Eq. 23 leads to

$$k_{\text{VSC}} \approx \frac{1}{N} \cdot 4Ng_c^2\omega_c^2 \cdot \frac{\tau_c^{-1}\omega_0}{\left(\omega_c^2 - \omega_0^2\right)^2 + \tau_c^{-2}\omega_0^2} \cdot e^{-\beta\hbar\omega_c}, \tag{30}$$

where in the second line we have explicitly approximated $n(\omega_c) \approx e^{-\beta\hbar\omega_c}$. As a special case of Eq. 30, when $\omega_c = \omega_0$, Eq. 30 becomes

$$k_{\text{VSC}} = \frac{1}{N}\Omega_{\text{R}}^2 \cdot \tau_c \cdot e^{-\beta\hbar\omega_0}, \tag{31}$$

where $\Omega_{\text{R}} = 2\sqrt{N}g_c \cdot \sqrt{\omega_0}$. The cavity quality factor is often defined as $Q = \tau_c^{-1}\omega_0$ for the resonance condition. For the recent VSC experiment by Ebbesen [3], the typical values for these parameters are $\tau_c \approx 100$ fs (reading from a width of $\Gamma_c = \tau_c^{-1} \approx 53$ cm^{-1} of the cavity transmission spectra). If the cavity frequency $\omega_c = \omega_0 = 1200$ cm^{-1}, then the quality factor is $Q \approx 22.6$. However, for the current theory, the overall rate constant would not explicitly depend on N (Eq. 30), meaning that only for the small N and strong coupling between molecules and the cavity mode there will be an appreciation amount of the cavity-modified effect. This is in contrast to the experimental observation of the collective effect and should be viewed as a major limitation of current theory.

When considering the disorder of the orientation between the dipole and the cavity field polarization direction, $\left|\langle\nu_k|\hat{\mathcal{S}}|G\rangle\right|^2 = \mu_{\text{LL}'}^2 \cdot \cos^2\varphi_k$, the FGR rate in Eq. 30 becomes $k_{\text{VSC}} = \frac{2}{\hbar}\mu_{\text{LL}'}^2 \langle\cos^2\varphi\rangle \cdot J_{\text{eff}}(\omega_0) \cdot n(\omega_0)$ upon statistical averaging of dipole orientations. For fully isotropically distributed dipoles, $\langle\cos^2\varphi\rangle = 1/3$.

3.4 Resonance Behavior of k_{VSC}.

We want to demonstrate the numerical behavior of the current theory predicted by Eq. 23 and 29. Because the current theory lacks the collective effect, we take the $N = 1$ limit and scale up the coupling strength between a single molecule and the cavity mode, as most previous work does [22, 23, 39]. This leads to the expression of

$$k_{\text{VSC}}^{\text{1D}} = \Omega_{\text{R}}^2 \cdot \frac{\omega_c\tau_c^{-1}\omega_0}{\left(\omega_c^2 - \omega_0^2\right)^2 + \tau_c^{-2}\omega_0^2} \cdot e^{-\beta\hbar\omega_0} \tag{32}$$

under the single mode limit (or under the 1D cavity case, see Eq. 23). As expected, the k_{VSC} expression in Eq. 30 should contain several characteristic physical constants, including the speed of light c in ω_c (see Eq. 3) as it is related to light-matter interaction, Planck's constant $\hbar$ in g_c (see Eq. 9) as it should be a quantum theory, and Boltzmann's constant k_{B} in $n(\omega_0)$ as it is a thermally activated theory. We adopt a model system used in Ref. 39 to demonstrate the basic trend of k_{VSC} predicted by the current theory. The schematic of the model is provided in Fig. 2, whereas the details are provided in Supplementary Material, Sec II.

To obtain the numerically exact rate constant for the same model, we use hierarchical equations of motion (HEOM) to simulate the population dynamics and obtain the VSC-modified rate constant, with the details provided in Sec. VII of the Supplementary Material. The HEOM simulation requires a linear system-bath coupling Hamiltonian. To this end, we follow the previous work [22, 39] and assume that the dipole operator is linear, $\mu(\hat{R}) = \hat{R}$. As a result, the light-matter coupling term in Eq. 1 (for a single molecule case) is simplified as $\omega_c\hat{q}_c\lambda \cdot \mu(\hat{R}) = \omega_c\lambda\hat{q}_c\hat{R}$. Further, we follow Ref. 39 by defining the normalized light-matter coupling strength as below,

$$\eta_c = \sqrt{\frac{1}{2\hbar\omega_c}}\lambda = \frac{\Omega_{\text{R}}}{2\omega_c\mu_{\text{LL}'}}. \tag{33}$$

We use a similar range of η_c as used in Ref. 39. For the FGR-based theory (Eq. 32), we use the value of the k_0 (outside the cavity rate constant) obtained from the HEOM simulation and report $k/k_0 = 1 + k_{\text{VSC}}/k_0$. The

forward rate constant is obtained by evaluating [39, 47]

$$k = -\lim_{t \to t_{\mathrm{p}}} \frac{\dot{P}_{\mathcal{R}}(t)}{P_{\mathcal{R}}(t) + \chi_{\mathrm{eq}} \cdot [P_{\mathcal{R}}(t) - 1]}, \qquad (34)$$

where $\chi_{\mathrm{eq}} \equiv P_{\mathcal{R}}/P_{\mathcal{P}}$ denotes the ratio of equilibrium population between the reactant and product, see Sec. VII of the Supplementary Material.
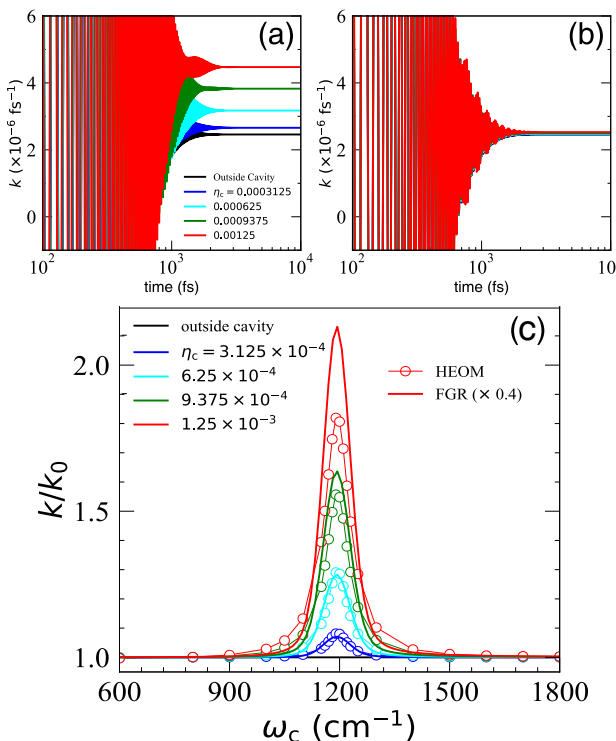

Fig. 5: Numerically exact simulation and the analytic FGR results of the rate constant. (a) The flux-side correlation functions computed by HEOM at resonance (with $\omega_{\mathrm{c}} = \omega_0 = 1190$ cm^{-1}). (b) The flux-side correlation functions are calculated by HEOM but off-resonance (with $\omega_{\mathrm{c}} = 1000$ cm^{-1}). (c) The profile of the resonant VSC rate constant k/k_0 as a function of ω_{c} with different light-matter coupling strengths, η_{c}, obtained by FGR (solid lines) and HEOM simulations (open circles with guiding thin lines), respectively. The cavity lifetime is set to be $\tau_{\mathrm{c}} = 200$ fs.

The time derivative $\dot{P}_{\mathcal{R}}(t)$ in Eq. 34 is evaluated numerically. For the symmetric double potential model considered in this work, $\chi_{\mathrm{eq}} = 1$. The limit $t \to t_{\mathrm{p}}$ represents that the dynamics have already entered the rate process regime (linear response regime) and t_{p} represents the "plateau time" of the time-dependent rate which is equivalent to a flux-side time correlation function formalism. One can also view Eq. 34 as the flux-side correlation function that provides the time-dependent rate constant $k(t)$, which captures both the initial transient dynamics (the oscillatory behaviors

of $k(t)$) and the longer time rate process (plateau of $k(t_{\mathrm{p}})$). We report the numerical value of k/k_0 as a function of the cavity frequency ω_{c}. For the rate constant predicted by FGR, we only report the value of $k/k_0 = 1 + k_{\mathrm{VSC}}/k_0$ (see Eq. 11) and we directly use the numerical result of k_0 obtained from the HEOM simulation.

Fig. 5 presents the numerical simulations of the rate constant from HEOM as well as the FGR results. Fig. 5a presents $k(t)$ for the resonant case when $\omega_{\mathrm{c}} = \omega_0$, at various light-matter coupling strengths η_{c}. One can clearly see the plateau value of $k(t)$ increases as η_{c} increases. Fig. 5b presents the case where $\omega_{\mathrm{c}} < \omega_0$ where $\omega_{\mathrm{c}} = 1000$ cm^{-1}, and there is no apparent η_{c} dependence of $k(t)$, indicating that there is no effect of coupling to the cavity. Fig. 5c presents the value of k/k_0 (scaled by 0.4) as changing ω_{c} using Eq. 30, depicted by the thick solid lines. A range of light-matter coupling strength η_{c} is explored. The FGR expression shows the sharp resonance behavior of the VSC-modified rate profile at $\omega_{\mathrm{c}} = \omega_0 = 1190$ cm^{-1}. A similar sharp resonance has been observed in VSC experiments [1, 5, 6] and quantum dynamics simulations [39]. Further, we provide the rate constant calculated from the numerically exact HEOM simulations (see Sec. VII of the Supplementary Material), depicted by the open circles with a thin guiding line. Although the analytic FGR expression overestimates the rate constant by about two times, the overall agreement between the FGR expression and the HEOM numerical results is remarkable, across the range of ω_{c} and η_{c} we explored.

Next, we explicitly consider going beyond the single-mode limit. For the 1D FP cavity, k_{VSC} still reduces back to the single-mode approximation. For the 2D FP cavity, based on the expression in Eq. 14 and Eq. 29, the VSC-modified rate constant is expressed as

$$k_{\mathrm{VSC}}^{\mathrm{2D}} = \frac{2g_{\mathrm{c}}^2}{\pi \mathcal{Z}_{\mathrm{eff}} \xi} \int_{\omega_{\mathrm{c}}}^{\omega_{\mathrm{m}}} d\omega_{\mathbf{k}} \; \frac{\omega_{\mathbf{k}} e^{-\beta \hbar \omega_{\mathbf{k}}}}{1 + (\tau_{\mathrm{c}}/\tau_{\|})} \cdot \frac{\omega_{\mathbf{k}}^2 \tau_{\mathrm{c}}^{-1} \omega_0 \cdot n(\omega_0)}{\left(\omega_{\mathbf{k}}^2 - \omega_0^2\right)^2 + \tau_{\mathrm{c}}^{-2} \omega_0^2}, \qquad (35)$$

where $\tau_{\|} = \omega_{\mathbf{k}} \mathcal{D} / \left[c \sqrt{\omega_{\mathbf{k}}^2 - \omega_{\mathrm{c}}^2}\,\right]$ (c.f. Eq. 26), and ξ is expressed in Eq. 25. Note that this expression also peaks at $\omega_{\mathrm{c}} = \omega_0$ (as indicated in Fig. 4c), when $\tau_{\|} \to \infty$. In Eq. 35, ω_{c} is the lower limit of the integral with respect to $d\omega_{\mathbf{k}}$, as well as appearing explicitly in $\tau_{\|}$. The result of this definite integral in Eq. 35 is *not* as simple as replacing $\omega_{\mathbf{k}}$ with ω_{c} as in the single-mode approximation (Eq. 32).
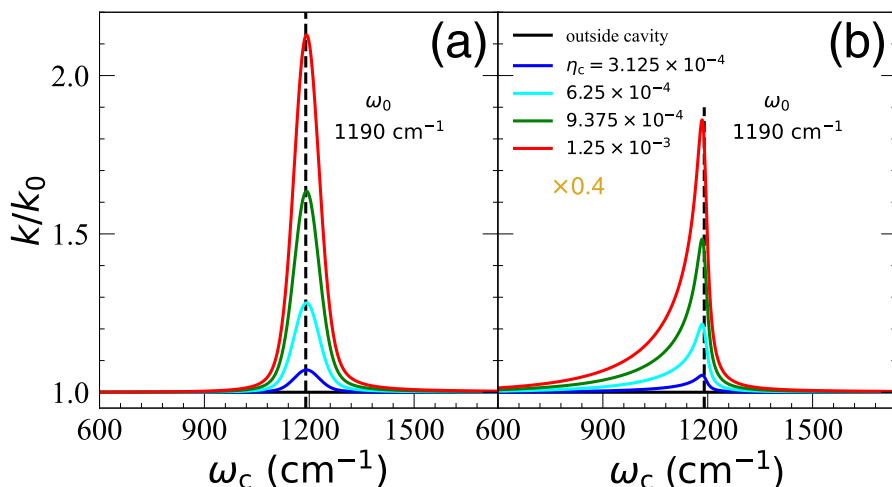
Fig. 6: FGR rate profiles of k/k_0 as a function of ω_c. (a) FGR rate using $k_{\mathrm{VSC}}^{\mathrm{1D}}$ (Eq. 32) for the single mode case (or the many modes case inside a 1D FP cavity) calculated using Eq. 32 (same as the solid lines in Fig. 5c). (b) FGR rate profiles $k_{\mathrm{VSC}}^{\mathrm{2D}}$ (Eq. 35 for many mode cases inside a 2D FP cavity. Here, we use $\mathcal{D}/c = 1$ fs, which corresponds to the cavity diameter $\mathcal{D} = 0.3$ μm. Note that both $k_{\mathrm{VSC}}^{\mathrm{1D}}$ and $k_{\mathrm{VSC}}^{\mathrm{2D}}$ are rescaled by a factor of 0.4 to be consistent with Fig. 5.

Fig. 6 presents the FGR rates under different η_c values. Fig. 6a is the same as Fig. 5a, which corresponds to the single-mode case (or the many-mode case inside a 1D FP cavity). Fig. 6b presents the estimated value of k/k_0 using k_{VSC} expression in Eq. 35, corresponding to the case of many modes inside a 2D FP cavity. Here, we choose $\mathcal{D}/c = 1$ fs, which corresponds to $\mathcal{D} = 0.3$ μm. The numerical integration scheme is the same as the calculation of $\mathcal{A}(\omega)$, and the convergence is carefully checked. One can observe that the resonance peak is still centered around $\omega_c = \omega_0$, which demonstrates the normal incidence condition. The resonance peak is asymmetric due to the asymmetry of $\mathcal{A}(\omega)$ (see Figs. 4c and f). Moreover, the rate profile tails toward the lower energy regions, which is the opposite of the trend in $\mathcal{A}(\omega)$ (see Fig. 4). Compared to the single mode version of the theory, considering many modes in a 2D FP cavity predicts that the "action spectrum" of the VSC-modified rate constant has an asymmetric behavior around $\omega_c = \omega_0$, with a longer tail when $\omega_c < \omega_0$. This is an interesting prediction from the current theory in Eq. 35. In recent VSC experiments by Simpkins [8], it does seem that the $\omega_c < \omega_0$ side has a longer tail than the $\omega_c > \omega_0$ side of the action spectrum (k_{VSC} vs ω_c plot, see Fig. 3A of Ref. 8). However, this could be due to the lack of more experimental data points for a blue-tuned cavity ($\omega_c > \omega_0$) due to the experimental difficulty. More experimental data are required to definitively test this trend.

4 Conclusion

We present a theory to explain the current VSC experiments, focusing on the origin of the resonance condition at normal incidence. The theory clearly explains the resonance condition for the observed VSC effect and provides an explanation of why the resonant effect occurs only at the normal incident angle. In particular, we find that the cavity-modified rate constant k_{VSC} can be expressed as the coupling strength multiplied by the accumulated spectral function $\mathcal{A}(\omega)$ of the cavity, where $\mathcal{A}(\omega)$ peaks at ω_c (when $k_\parallel = 0$, *i.e.*, bottom of the dispersion band). For a 1D FP cavity, this is caused by a van-Hove-type singularity (Eq. 22) in the DOS of the photonic modes. For a 2D FP cavity, we found that one needs to additionally consider the photon loss associated with $k_\parallel$ direction (Eq. 26), which creates the peak of $\mathcal{A}(\omega)$ at ω_c. As such, the oblique incidence still has the spectral function peaked at the ω_c, not at the higher incident angle. This theory explains why Rabi splitting is not a *sufficient condition* to achieve a VSC modified rate effect, providing a new insight into the mechanistic understanding of VSC modification.

Under the normal incidence condition, k_{VSC} will peak at $\omega_c = \omega_0$. For the 1D cavity case, k_{VSC} naturally reduces to the single-mode case (Eq. 32), and we have directly compared the FGR analytic expression with the numerically exact rate constant for a single molecule under strong coupling, which provides agreement across a range of light-matter coupling strengths

and cavity frequencies. For the 2D cavity case, we evaluated the FGR rate expression (Eq. 35), and found a similar sharp resonance at $\omega_c = \omega_0$ compared to the single mode (or the 1D case), with an asymmetric rate constant profile and a long tail when $\omega_c < \omega_0$. This is a unique prediction from the current theory, which should be checked with future experiments.

On the other hand, the current theory cannot explain the observed collective effect, and only when a few molecules are strongly coupled to the cavity can the current theory predict the cavity modifications to the rate constant. This is the limitation of the current theory, and future work is needed to fully address these issues. However, current work provides significant progress toward building the ultimate theory for understanding VSC effects. Future work will focus on developing a microscopic theory that can explain the collective effect.

Supplementary Material

See Supplementary Material for additional information on detailed derivations of the Hamiltonian; details of the molecular system; analysis of the Rabi splitting; the effective Hamiltonian and effective spectral density derived by applying harmonic analysis to classical equations of motion; derivation of the VSC-modified rate constant expression in Eq. 14 of the main text; DOS analysis for the 1D and 2D FP cavity; details of the quantum dynamics simulation results.

Acknowledgement

Data Availability

The data that support the findings of this work are available from the corresponding author under reasonable request.

References

[1] A. Thomas, J. George, A. Shalabney, M. Dryzhakov, S. J. Varma, J. Moran, T. Chervy, X. Zhong, E. Devaux, C. Genet, J. A. Hutchison, and T. W. Ebbesen, Ground-state chemical reactivity under vibrational coupling to the vacuum electromagnetic field, Angew. Chem. Int. Ed. **55**, 11462–11466 (2016).

[2] R. M. A. Vergauwe, A. Thomas, K. Nagarajan, A. Shalabney, J. George, T. Chervy, M. Seidel, E. Devaux, V. Torbeev, and T. W. Ebbesen, Modification of enzyme activity by vibrational strong coupling of water, Angew. Chem. Int. Ed. **58**, 15324–15328 (2019).

[3] A. Thomas, L. Lethuillier-Karl, K. Nagarajan, R. M. A. Vergauwe, J. George, T. Chervy, A. Shalabney, E. Devaux, C. Genet, J. Moran, and T. W. Ebbesen, Tilting a ground-state reactivity landscape by vibrational strong coupling, Science **363**, 615–619 (2019).

[4] A. Thomas, A. Jayachandran, L. Lethuillier-Karl, R. M. Vergauwe, K. Nagarajan, E. Devaux, C. Genet, J. Moran, and T. W. Ebbesen, Ground state chemistry under vibrational strong coupling: dependence of thermodynamic parameters on the rabi splitting energy, Nanophotonics **9**, 249–255 (2020).

[5] J. Lather, P. Bhatt, A. Thomas, T. W. Ebbesen, and J. George, Cavity catalysis by cooperative vibrational strong coupling of reactant and solvent molecules, Angew. Chem. Int. Ed. **58**, 10635–10638 (2019).

[6] J. Lather, A. N. K. Thabassum, J. Singh, and J. George, Cavity catalysis: modifying linear free-energy relationship under cooperative vibrational strong coupling, Chem. Sci. **13**, 195–202 (2022).

[7] K. Hirai, R. Takeda, J. A. Hutchison, and H. Ujiâi, Modulation of prins cyclization by vibrational strong coupling, Angew. Chem. Int. Ed. **59**, 5332–5335 (2020).

[8] W. Ahn, J. F. Triana, F. Recabal, F. Herrera, and B. S. Simpkins, Modification of ground state chemical reactivity via light-matter coherence in infrared cavities, Science **380**, 1165–1168 (2023).

[9] K. Gu, Q. Si, N. Li, F. Gao, L. Wang, and F. Zhang, Regulation of Recombinase Polymerase Amplification by Vibrational Strong Coupling of Water, ACS Photonics **10**, 1633–1637 (2023).

[10] J. Lather and J. George, Improving enzyme catalytic efficiency by co-operative vibrational strong coupling of water, J. Phys. Chem. Lett. **12**, 379–384 (2021).

[11] K. Hirai, J. A. Hutchison, and H. Uji-i, Recent progress in vibropolaritonic chemistry, ChemPlusChem **85**, 1981–1988 (2020).

[12] K. Nagarajan, A. Thomas, and T. W. Ebbesen, Chemistry under vibrational strong coupling, J. Am. Chem. Soc. **143**, 16877–16889 (2021).

[13] B. S. Simpkins, A. D. Dunkelberger, and I. Vurgaftman, Control, modulation, and analytical descriptions of vibrational strong coupling, Chem. Rev. **123**, 5020–5048 (2023).

[14] J. A. Campos-Gonzalez-Angulo, Y. R. Poh, M. Du, and J. Yuen-Zhou, Swinging between shine and shadow: Theoretical advances on thermally activated vibropolaritonic chemistry, J. Chem. Phys. **158**, 230901 (2023).

[15] J. Galego, C. Climent, F. J. Garcia-Vidal, and J. Feist, Cavity casimir-polder forces and their effects in ground-state chemical reactivity, Phys. Rev. X **9**, 021057 (2019).

[16] J. A. Campos-Gonzalez-Angulo, R. F. Ribeiro, and J. Yuen-Zhou, Resonant catalysis of thermally activated chemical reactions with vibrational polaritons, Nat. Commun. **10**, 4685 (2019).

[17] A. Semenov and A. Nitzan, Electron transfer in confined electromagnetic fields, J. Chem. Phys. **150**, 174122 (2019).

[18] I. Vurgaftman, B. S. Simpkins, A. D. Dunkelberger, and J. C. Owrutsky, Negligible effect of vibrational polaritons on chemical reaction rates via the density of states pathway, J. Phys. Chem. Lett. **11**, 3557–3562 (2020).

[19] T. E. Li, A. Nitzan, and J. E. Subotnik, On the origin of ground-state vacuum-field catalysis: Equilibrium consideration, J. Chem. Phys. **152**, 234107 (2020).

[20] V. P. Zhdanov, Vacuum field in a cavity, light-mediated vibrational coupling, and chemical reactivity, Chem. Phys. **535**, 110767 (2020).

[21] J. A. Campos-Gonzalez-Angulo and J. Yuen-Zhou, Polaritonic normal modes in transition state theory, J. Chem. Phys. **152**, 161101 (2020).

[22] X. Li, A. Mandal, and P. Huo, Cavity frequency-dependent theory for vibrational polariton chemistry, Nat. Commun. **12**, 1315 (2021).

[23] C. Schäfer, J. Flick, E. Ronca, P. Narang, and A. Rubio, Shining light on the microscopic resonant mechanism responsible for cavity-mediated chemical reactivity, Nat. Commun. **13**, 7817 (2022).

[24] X. Li, A. Mandal, and P. Huo, Theory of mode-selective chemistry through polaritonic vibrational strong coupling, J. Phys. Chem. Lett. **12**, 6974–6982 (2021).

[25] T. E. Li, A. Nitzan, and J. E. Subotnik, Collective vibrational strong coupling effects on molecular vibrational relaxation and energy transfer: Numerical insights via cavity molecular dynamics simulations, Angew. Chem. Int. Ed. **60**, 15533–15540 (2021).

[26] T. E. Li, A. Nitzan, and J. E. Subotnik, Polariton relaxation under vibrational strong coupling: Comparing cavity molecular dynamics simulations against fermiâs golden rule rate, J. Chem. Phys. **156**, 134106 (2022).

[27] A. Mandal, X. Li, and P. Huo, Theory of vibrational polariton chemistry in the collective coupling regime, J. Chem. Phys. **156**, 014101 (2022).

[28] M. Du and J. Yuen-Zhou, Catalysis by dark states in vibropolaritonic chemistry, Phys. Rev. Lett. **128**, 096001 (2022).

[29] J. P. Philbin, Y. Wang, P. Narang, and W. Dou, Chemical reactions in imperfect cavities: Enhancement, suppression, and resonance, J. Phys. Chem. C **126**, 14908–14913 (2022).

[30] D. S. Wang, T. Neuman, S. F. Yelin, and J. Flick, Cavity-modified unimolecular dissociation reactions via intramolecular vibrational energy redistribution, J. Phys. Chem. Lett. **13**, 3317–3324 (2022).

[31] D. S. Wang, J. Flick, and S. F. Yelin, Chemical reactivity under collective vibrational strong coupling, J. Chem. Phys. **157**, 224304 (2022).

[32] J. Sun and O. Vendrell, Suppression and enhancement of thermal chemical rates in a cavity, J. Phys. Chem. Lett. **13**, 4441–4446 (2022).

[33] E. W. Fischer, J. Anders, and P. Saalfrank, Cavity-altered thermal isomerization rates and dynamical resonant localization in vibro-polaritonic chemistry, J. Chem. Phys. **156**, 154305 (2022).

[34] L. P. Lindoy, A. Mandal, and D. R. Reichman, Resonant cavity modification of ground-state chemical kinetics, J. Phys. Chem. Lett. **13**, 6580–6586 (2022).

[35] S. Mondal, D. S. Wang, and S. Keshavamurthy, Dissociation dynamics of a diatomic molecule in an optical cavity, J. Chem. Phys. **157**, 244109 (2022).

[36] J. Cao, Generalized resonance energy transfer theory: Applications to vibrational energy flow in optical cavities, J. Phys. Chem. Lett. **13**, 10943–10951 (2022).

[37] K. S. U. Kansanen and T. T. Heikkilä, Cavity-induced bifurcation in classical rate theory, arXiv , 10.48550/arXiv.2202.12182 (accessed 2023–05–12) (2023).

[38] M. Du, Y. R. Poh, and J. Yuen-Zhou, Vibropolaritonic reaction rates in the collective strong coupling regime: Pollakâgrabertâhänggi theory, J. Phys. Chem. C **127**, 5230–5237 (2023).

[39] L. P. Lindoy, A. Mandal, and D. R. Reichman, Quantum dynamical effects of vibrational strong coupling in chemical reactivity, Nat. Commun. **14**, 2733 (2023).

[40] M. C. Anderson, E. J. Woods, T. P. Fay, D. J. Wales, and D. T. Limmer, On the mechanism of polaritonic rate suppression from quantum transition paths, The Journal of Physical Chemistry Letters **14**, 6888–6894 (2023).

[41] M. R. Fiechter, J. E. Runeson, J. E. Lawrence, and J. O. Richardson, How quantum is the resonance behavior in vibrational polariton chemistry? The Journal of Physical Chemistry Letters **14**, 8261–8267 (2023).

[42] D. S. Wang and S. F. Yelin, A roadmap toward the theory of vibrational polariton chemistry, ACS Photonics **8**, 2818–2826 (2021).

[43] D. Sidler, M. Ruggenthaler, C. Schäfer, E. Ronca, and A. Rubio, A perspective on ab initio modeling of polaritonic chemistry: The role of non-equilibrium effects and quantum collectivity, J. Chem. Phys. **156**, 230901 (2022).

[44] A. Mandal, M. A. Taylor, B. M. Weight, E. R. Koessler, X. Li, and P. Huo, Theoretical advances in polariton chemistry and molecular cavity quantum electrodynamics, Chemical Reviews **123**, 9786–9879 (2023) .

[45] I. Vurgaftman, B. S. Simpkins, A. D. Dunkelberger, and J. C. Owrutsky, Comparative analysis of polaritons in bulk, dielectric slabs, and planar cavities with implications for cavity-modified reactivity, J. Chem. Phys. **156**, 034110 (2022).

[46] R. F. Ribeiro, Multimode polariton effects on molecular energy transport and spectral fluctuations, Communications Chemistry **5** (2022), 10.1038/s42004-022-00660-0.

[47] W. Ying and P. Huo, Resonance theory and quantum dynamics simulations of vibrational polariton chemistry, J. Chem. Phys. **159**, 084104 (2023).

[48] J. J. Hopfield, Theory of the contribution of excitons to the complex dielectric constant of crystals, Phys. Rev. **112**, 1555–1567 (1958).

[49] M. Tavis and F. Cummings, Exact solution for an n-molecule-radiation-field hamiltonian, Phys. Rev. **170**, 379–384 (1968).

[50] E. Jaynes and F. Cummings, Comparison of quantum and semiclassical radiation theories with application to the beam maser, Proc. IEEE **18**, 89–109 (1963).

[51] J. del Pino, J. Feist, and F. J. Garcia-Vidal, Quantum theory of collective strong coupling of molecular vibrations with a microcavity mode, New J. Phys. **17**, 053040 (2015).

[52] P. Hänggi, P. Talkner, and M. Borkovec, Reaction-rate theory: fifty years after kramers, Rev. Mod. Phys. **62**, 251–341 (1990).

[53] E. Pollak, H. Grabert, and P. Hänggi, Theory of activated rate processes for arbitrary frequency dependent friction: Solution of the turnover problem, J. Chem. Phys. **91**, 4073–4087 (1989).

[54] A. J. Leggett, Quantum tunneling in the presence of an arbitrary linear dissipation mechanism, Phys. Rev. B **30**, 1208–1218 (1984).

[55] A. Garg, J. N. Onuchic, and V. Ambegaokar, Effect of friction on electron transfer in biomolecules, J. Chem. Phys. **83**, 4491–4503 (1985).

[56] M. Thoss, H. Wang, and W. H. Miller, Self-consistent hybrid approach for complex systems: Application to the spin-boson model with debye spectral density, J. Chem. Phys. **115**, 2991–3005 (2001).

[57] L. V. Hove, The occurrence of singularities in the elastic frequency distribution of a crystal, Phys. Rev. **89**, 1189–1193 (1953).

[58] A. Shalabney, J. George, J. Hutchison, G. Pupillo, C. Genet, and T. W. Ebbesen, Coherent coupling of molecular resonators with a microcavity mode, Nature Communications **6**, 5981 (2015).

[59] B. Xiang, R. F. Ribeiro, M. Du, L. Chen, Z. Yang, J. Wang, J. Yuen-Zhou, and W. Xiong, Intermolecular vibrational energy transfer enabled by microcavity strong light-matter coupling, Science **368**, 665–667 (2020)
.